AGU PUBLICATIONS

JGR

Journal of Geophysical Research: Space Physics

TECHNICAL REPORTS: METHODS

10.1002/2015JA021723

An effective TEC data detrending method for the study of equatorial plasma bubbles and traveling ionospheric disturbances

Rezy Pradipta[1], Cesar E. Valladares[1], and Patricia H. Doherty[1]

[1]Institute for Scientific Research, Boston College, Chestnut Hill, Massachusetts, USA

Key Points:
- Special TEC detrending method based on a mechanical analogy of rolling barrel
- We have reliable differentiation between bubbles/depletions and wavelike features
- Application in mapping the full geographic profiles of equatorial plasma bubbles

Supporting Information:
- Supporting Information S1
- Movie S1

Correspondence to:
R. Pradipta,
rezy.pradipta@bc.edu

Citation:
Pradipta, R., C. E. Valladares, and P. H. Doherty (2015), An effective TEC data detrending method for the study of equatorial plasma bubbles and traveling ionospheric disturbances, *J. Geophys. Res. Space Physics*, *120*, 11,048–11,055, doi:10.1002/2015JA021723.

Received 24 JUL 2015
Accepted 14 NOV 2015
Accepted article online 18 NOV 2015
Published online 16 DEC 2015

Abstract Using a mechanical analogy of rolling a cylindrical barrel on a rough uneven surface, we developed a special method for detrending the GPS-derived total electron content (TEC) data. This method is specifically designed to recognize the presence of depletions in the TEC time series data and handle them differently from wavelike features. We also demonstrate a potential application of this technique to map the detailed geographic profile of TEC depletions over the equatorial region, using the South American sector as an example.

1. Introduction

In this work, we are introducing a special method for effectively detrending the total electron content (TEC) data that are routinely recorded by ground-based GPS receiver stations. The main emphasis of this TEC data detrending method is to recognize depletions (i.e., negative excursions) and distinguish them from wavelike phenomena (i.e., oscillatory signal). Hence, this technique could be particularly well suited for the equatorial region where the occurrence of ionospheric plasma bubbles is quite prevalent. It would also be applicable for the study of acoustic-gravity waves (AGW) and traveling ionospheric disturbances (TID) in general.

Figure 1 illustrates the intended purpose of this TEC data detrending method, using a set of artificially constructed signal. The synthesized signal consists of two wavelike features (W1 and W2) plus two separate depletions (D1 and D2) that are superposed on top of a more slowly varying background signal. Given such TEC time series, a successful TEC data detrending procedure can be expected to produce an inferred overall trend that broadly resembles the red curve shown in Figure 1 (top). Namely, the inferred trend should trace the null/equilibrium level (in between the crests and valleys) of the wavelike oscillations, and in addition, it should not fall down into the wide/deep valley of the depletions. Using the appropriately inferred trend, we would be able to isolate both depletion and wavelike features—as illustrated graphically in Figure 1 (bottom).

The merit of having such an effective TEC data detrending technique is quite evident. The study of AGW/TID [e.g., *Tsugawa et al.*, 2003; *Nicolls et al.*, 2004; *Tsugawa et al.*, 2011], equatorial plasma bubbles [e.g., *Haase et al.*, 2011; *Seemala and Valladares*, 2011; *Takahashi et al.*, 2015], and other types of anomalous features in the GPS TEC data would often rely crucially on the TEC data detrending process to determine a logical baseline. The TEC detrending process itself might not be so trivial due to a number of contributing factors. However, this very complexity also helps us narrow down the search for suitable TEC detrending methods.

First of all, the GPS TEC data themselves generally have some level of seasonal as well as day-to-day variability that would be too difficult to handle using climatology or quiet day curve(s) alone. For example, *Rishbeth and Mendillo* [2001] found that the variability in ionospheric *F* layer largely originates from a combination of solar, geomagnetic, and meteorological activities—which renders an ionospheric quiet day curve highly impractical. Furthermore, baselines derived from different ionospheric models often show some significant disagreement [e.g., *Mendillo et al.*, 2002; *Carter et al.*, 2013], thus making them less meaningful for data detrending purposes. Hence, it would arguably be better to infer the most reasonable trend/baseline plainly based on the factual characteristics of the GPS TEC data in hand. Some of the most widely used TEC data detrending techniques include the following: polynomial fit [e.g., *Kamogawa and Kakinami*, 2013; *Pradipta et al.*, 2014], moving average [e.g., *Tsugawa et al.*, 2007; *Nishioka et al.*, 2013], and wavelet or other types of filtering [e.g., *Borries et al.*, 2009; *Skone*, 2009; *Galvan et al.*, 2011].

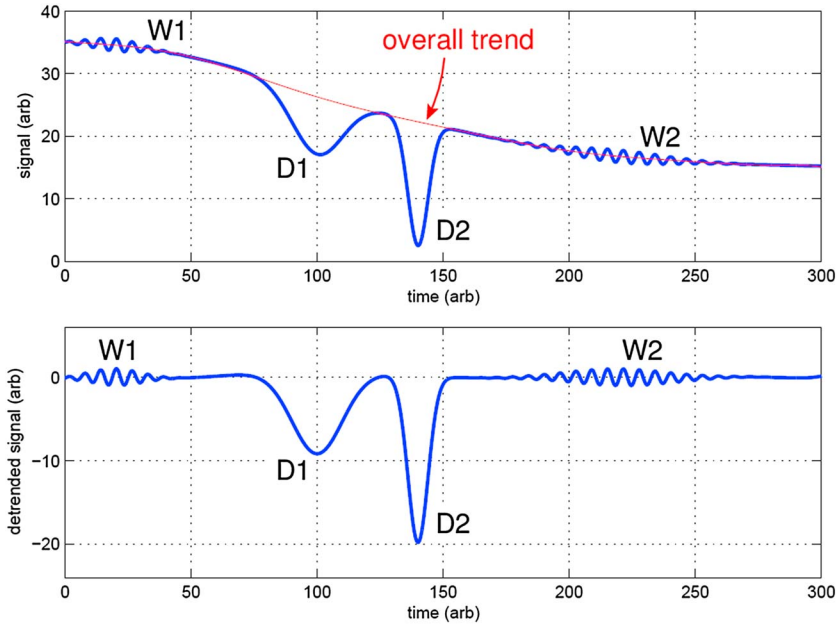

Figure 1. A schematic illustration of the essential functionality of this TEC data detrending procedure. Two wavelike features (W1 and W2) plus two depletions (D1 and D2) are present in the original synthesized signal, and the appropriately inferred overall trend allows us to isolate both types of features.

In the context of our present discussion, we face the challenge of distinguishing between depletions and wavelike features. Problems typically arise when we attempt to detrend the data using simple polynomial fit and/or moving average, since the TEC depletions are often mistaken as large-amplitude wave oscillations. While one might be able to manually exclude segment(s) of the data that contain depletions beforehand, manual interventions would generally render automated bulk data processing unfeasible. It is therefore desirable to have a numerical data detrending method that can inherently recognize the presence of depletions in the signal.

We resolve this problem by treating the signal shape as some form of terrain and rolling an imaginary barrel over this "terrain" to trace the upper envelope of the overall signal. With a sufficiently large radius, this "barrel" will roll over the depletions and will not fall down into the "valley" areas. By noting the location of these valley areas in the process, we can (temporarily) remove part(s) of the signal that correspond to depletions and replace them with a bridge/connecting curve constructed from the traced upper envelope. We will subsequently use this "depletion-free" signal to derive the overall trend via a more conventional method (e.g., polynomial fit or filtering).

Based on its working principles, we may refer to this numerical procedure as *mechanical rotary motion-implicit terrain* (MRMIT) filtering. The detailed formulation of this method as well as some illustrative examples are presented in the following sections below.

2. Basic Principles

As outlined above, this TEC data detrending procedure is based on a mechanical analogy of a cylindrical barrel rolling on a rough terrain. At a basic level, the procedure can be summarized as follows:

1. The complete set of contact points between the barrel and the terrain of signal values would trace a curve that defines an upper envelope of this signal.
2. Using the traced upper envelope, we can construct an intermediate depletion-free signal by replacing the depletions with bridge/connecting curves that effectively bypass the depletion valleys.
3. Since this intermediate depletion-free signal most likely contains only wavelike features on top of the slowly varying background (i.e., no depletions/bubbles), a more straightforward method (e.g., polynomial fit or filtering) can be safely used on it to infer an accurate overall trend.
4. Once we obtain the overall smooth trend in TEC, we can then compute the detrended TEC signal by subtracting the inferred TEC trend from the original unmodified TEC signal.

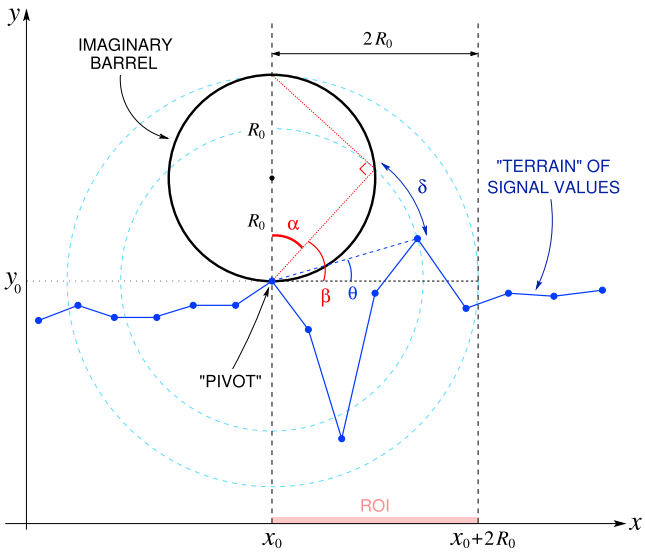

Figure 2. The basic geometry of an imaginary barrel rolling on a terrain of signal values. The barrel will pivot around its current contact point, and the next contact point would be the one with the smallest angular distance δ with respect to the leading edge of the rolling barrel (unless it is actually located outside of the $2R_0$ circle).

Note that the bridge/connecting curves are derived directly from the traced upper envelope, which in general would not sink into depletion valleys if we set the barrel size appropriately.

Figure 2 depicts the basic geometry of an imaginary barrel rolling on a terrain of discrete signal values. The terrain itself is formed by scaling the TEC time series data into an *xy* space where $x = \text{time}/\tau_0$ and $y = \text{TEC}/\zeta_0$. In practice, typical scaling factors might be $\tau_0 = 2$ h and $\zeta_0 = 40$ total electron content unit (TECU; 1 TECU = 10^{16} electrons/m^2). In this *xy* space, the radius of the barrel might also be fixed at unity for simplicity. Furthermore, in this mechanical analogy we will assume that the barrel always rolls perfectly without slipping and does not bounce on impact (i.e., any collision with the terrain is completely inelastic).

As the barrel rolls on top of this terrain, at any stage it will rest on a contact point and pivot around this center of rotation. The barrel then rolls forward until it lands on the next contact point. Geometrically, the next contact point would be the one with the smallest angular distance δ with respect to the leading edge of the barrel. This mechanical process continues with the next contact point serving as the new pivot.

Following the geometry depicted in Figure 2, we will denote the coordinate of the current contact point as (x_0, y_0) and the radius of the barrel as R_0. The main region of interest (ROI) for finding the next contact point is the interval $x_0 < x \le x_0 + 2R_0$. For convenience, the coordinate of any data point within this ROI can be denoted as $(x_0+\Delta x,\ y_0+\Delta y)$. Nominally, we set the imaginary barrel to rest upright on top of its current pivot point so that the line connecting the contact point and the center of the barrel is vertical. As also illustrated in Figure 2, the angular distance between a given data point in the ROI and the leading edge of the barrel is $\delta = \beta - \theta$. The angle θ is simply given by $\theta = \tan^{-1}(\Delta y/\Delta x)$. Meanwhile, the angle β can be determined via the angle $\alpha = 90° - \beta$; where we know from geometry that

$$\cos\alpha = \frac{\sqrt{(\Delta x)^2 + (\Delta y)^2}}{2R_0}. \tag{1}$$

Because in this case we have $\cos\alpha = \sin\beta$, then the full expression for the angular distance δ becomes

$$\delta = \sin^{-1}\left[\frac{\sqrt{(\Delta x)^2 + (\Delta y)^2}}{2R_0}\right] - \tan^{-1}\left[\frac{\Delta y}{\Delta x}\right]. \tag{2}$$

The above formulation had assumed that the data point is inside the $2R_0$ circle. If the data point is actually located outside the $2R_0$ circle, then we may simply take $\beta = 90°$ in that case. Among all the data points within the ROI, we will minimize the angular distance δ to determine the next contact point. If the ROI turns out to be empty, then we will simply designate the first data point past the ROI as the next contact point.

The resulting curve traced by all the contact points will be called the "barrel-roll curve" (BRC). At this point, we can safely revert from the *xy* space back into the TEC-versus-time representation. In this representation, the BRC is thus the desired upper envelope of the TEC time series signal. Based on the BRC, we will construct a band of TEC values that are bounded by two envelopes:

$$\text{BRC}_{\text{upper}} = \text{BRC} + \delta_1, \tag{3}$$

$$\text{BRC}_{\text{lower}} = \text{BRC} - \delta_2. \tag{4}$$

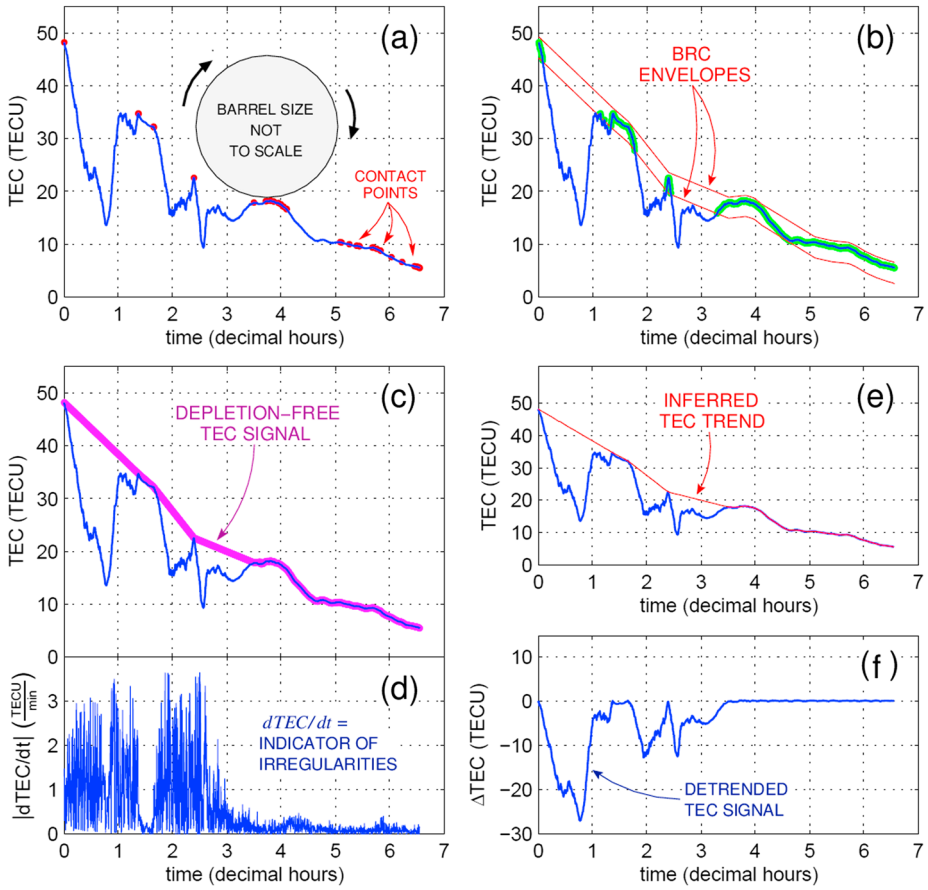

Figure 3. A real-data example illustrating each stage of the proposed TEC data detrending procedure. (a) Finding the contact points on the terrain of absolute TEC values to construct a barrel-roll curve or BRC for short. (b) Collecting additional points to close small gaps in between the contact points. (c and d) Forming the depletion-free TEC signal that excludes depletion features, using the dTEC/d*t* values as additional verification. (e) Inferring a smooth trend based on the depletion-free TEC signal. (f) The detrended TEC signal obtained by subtracting the inferred trend from the original TEC signal.

In practice, typical values for the offsets might be $\delta_1 = 1$ TECU and $\delta_2 = 3$ TECU, respectively. All points from the TEC time series data that fall within these two BRC envelopes will be collected to start forming the depletion-free signal. This operation (using the BRC envelopes) will certainly close many small gaps in between the identified contact points, but in general, it would still leave some larger gap(s). These larger gaps are the candidates for depletions in the TEC data.

In order to determine whether a particular gap is an actual depletion in the TEC data or not, we need to examine the values of dTEC/d*t* within that gap. Elevated dTEC/d*t* values would indicate the presence of some irregularities, and therefore, in that case we will decide to classify the gap as an actual depletion because turbulent structures are commonly found inside equatorial plasma bubbles [see, e.g., *McClure et al.*, 1977; *Basu et al.*, 1978; *Hysell et al.*, 1994; *Kil and Heelis*, 1998]. To perform the classification, we calculate the difference between the 95th percentile and the 5th percentile of |dTEC/d*t*| values within the gap. If this difference exceeds a fixed numerical cutoff of 0.8 TECU/min, we then classify the gap as a depletion. If a gap has been positively classified as a depletion, we will bridge over the gap using the BRC. Otherwise, if the gap is not a depletion, we are going to close the gap using the original TEC time series data from that time segment. Note also that the use of |dTEC/d*t*| indicator to mark turbulence and irregularities would generally suppress the possibility of creating "spurious/artificial depletions" in the final results. Without the |dTEC/d*t*| indicator, such error could have easily occurred when we encounter a rather sharp rise/enhancement in TEC, e.g., due to plasma blobs [*Pimenta et al.*, 2007]. After this stage has been completed, we will then obtain the finalized depletion-free signal.

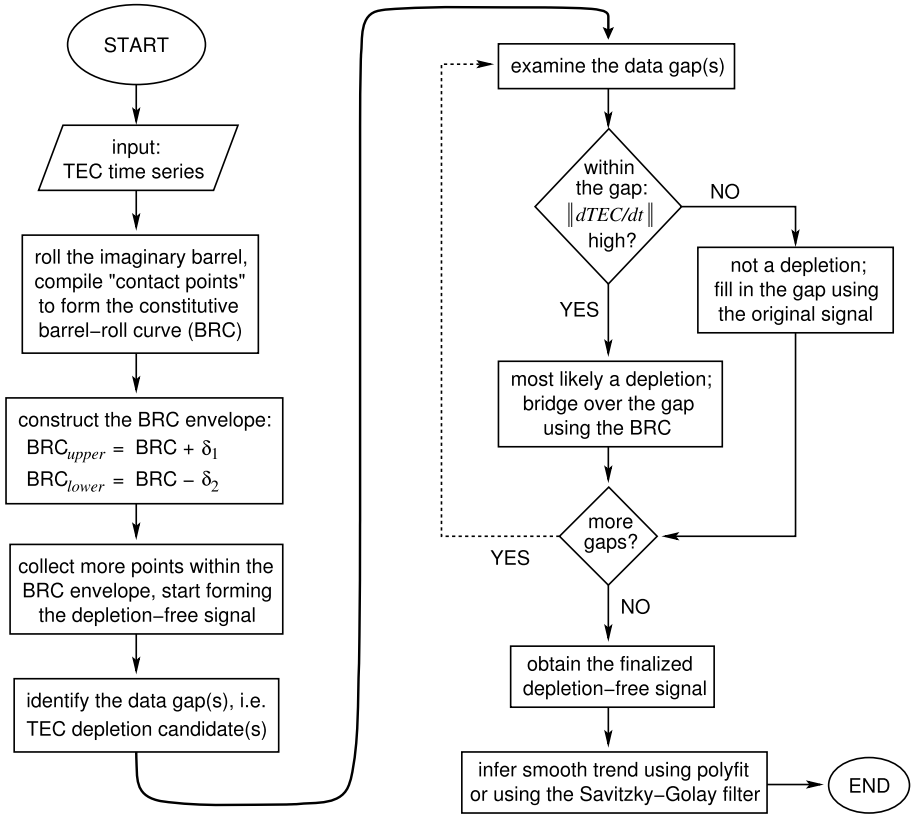

Figure 4. A simplified flow diagram of the proposed TEC data detrending procedure, detailing some of the steps illustrated in Figure 3.

Figure 4 depicts a simplified flow diagram that outlines our proposed TEC data detrending procedure as a whole. It details the essential steps/operations in this proposed TEC data detrending procedure, from start to end. This flow diagram also represents one of the simplest ways to implement this TEC detrending procedure in a routine/automated data analysis and processing system. Based on this basic outline, more complex variants can certainly be implemented in practice to meet specific needs and requirements.

Subsequently, the overall trend in the TEC data can be inferred by fitting a polynomial of suitable degree to this depletion-free signal. Savitzky-Golay filter [see, e.g., *Savitzky and Golay*, 1964; *Bromba and Ziegler*, 1981; *Persson and Strang*, 2003] can also be used on the depletion-free signal to infer the overall TEC trend. All of the above steps are made clearer in the next section via an illustrative example using a set of real TEC data.

3. Illustrative Example

Figure 3 shows a working example of the proposed TEC data detrending procedure, illustrating the different operations performed at various stages. This test example was done using a set of real TEC data recorded by a GPS receiver station (codename GVAL) in South America on 20 December 2011. In this case, the slant TEC was originally measured along the line-of-sight between the receiver and GPS PRN 21. The slant TEC has subsequently been converted into an equivalent vertical TEC. Hence, in this example we are always working with the equivalent vertical TEC values. Note also that here we have applied an offset to the time axis, and thus, the time $t = 0$ corresponds to the beginning of the GPS satellite pass in this example.

Figure 3a depicts the original TEC time series signal (blue curve) along with the identified contact points (red dots) of the rolling barrel. Note that the barrel shown in this graph is for the purpose of illustration only and was not drawn to scale. These contact points will be interpolated to form the barrel-roll curve (BRC), which can then be offset vertically upward/downward to construct the upper/lower BRC envelopes.

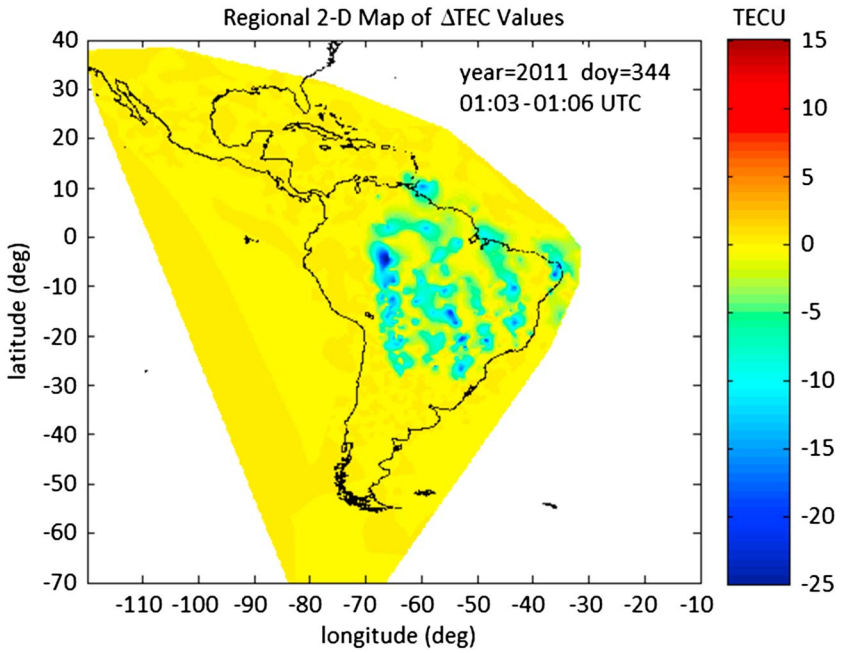

Figure 5. A 2-D geographic latitude/longitude map of gridded ΔTEC values over South America on 10 December 2011 at 01:03 UTC (with a 3-minute integration time), showing the spatial distribution of TEC depletions over the region. Before the data gridding, the ΔTEC values on each individual GPS satellite pass had been derived using the TEC data detrending procedure described in this manuscript.

Figure 3b shows the constructed BRC envelopes (red curves) in relation to the original TEC time series signal (blue curve). Portion of the TEC time series data that are contained within the two BRC envelopes have been highlighted green in this graph, and they form the initial configuration of the depletion-free signal.

Figure 3c shows the resulting depletion-free signal (magenta curve) together with the original TEC time series signal (blue curve). One would recognize that the depletions have been bridged using the BRC curve. The decision whether a gap should be filled in using the original TEC data or be bridged using the BRC are made using the dTEC/dt values as an additional source of cross verification, as shown in Figure 3d. One can see that for the time segments classified as depletions (i.e., where the depletion-free signal separates up from the original TEC time series data), the values of |dTEC/dt|, in general, were elevated significantly above the background level.

Figure 3e shows the inferred trend in TEC (red curve) obtained by applying a Savitzky-Golay filter on the depletion-free signal from the previous stage. The original TEC time series data are shown here as well (blue curve). By subtracting the inferred trend from the original data, we would obtain the detrended TEC signal. Finally, Figure 3f shows the detrended TEC signal that results.

In general, the output of this TEC data detrending procedure would depend on the selected values of the setup parameters (i.e., the barrel radius R_0, as well as the BRC offsets δ_1 and δ_2). By repeating the same analysis as above using different parameter values, we determined that this TEC detrending procedure is only mildly sensitive to the value of R_0 and δ_2, and is largely insensitive to the parameter δ_1. We found that R_0 between 0.8 and 1.3 produces essentially the same ΔTEC signal as the default setting of $R_0 = 1$. Beyond this interval, we start to see some notable deviation. We also found that δ_2 between 0.1 TECU and 3.3 TECU produces ΔTEC signal that is almost identical to the default setting of $\delta_2 = 3$ TECU (keeping $R_0 = 1$). Beyond this interval, some deviation starts to appear. Meanwhile, the detrending procedure is insensitive to the exact choice of δ_1 (as long as we keep $\delta_1 > 0$). A number of supplementary plots from these parameter sensitivity tests, plus a comparison with several other (more traditional) methods, are provided in the supporting information.

Finally, Figure 5 shows a 2-D geographic map of the TEC depletions that have been derived using this TEC data detrending procedure (an animation is also available in the supporting information Movie S1). The processing for this map was carried out using data collected from ~240 GPS receiver stations in the Caribbean, Central America, and South America. After the TEC data from each individual GPS satellite pass have been

fully detrended, the ΔTEC values are subsequently transferred from the ionospheric piercing point (IPP) trajectories into a regular latitude/longitude grid with 0.2°×0.2° spatial resolution. Here the IPP was set at an altitude of 350 km above the Earth's surface. The mapped ΔTEC values are indicated by a colormap, where yellow/orange color stands around the zero level and darker blue color corresponds to deeper depletions. The data gridding was performed using natural neighbor interpolation method [see, e.g., *Sibson*, 1981; *Sambridge et al.*, 1995] within the convex hull/boundary defined by the outermost data points. Note also that one should generally disregard the mapped ΔTEC values over the Pacific Ocean, as there are no real data from coordinate(s) located in the middle of open ocean.

Based on our observations, the $|dTEC/dt|$ values within the identified depletions are typically in the range of 1.5–3.0 TECU/min. Outside the depletions, we found that the $|dTEC/dt|$ values are mostly below 0.5 TECU/min. On this issue, a set of supplementary data maps of ΔTEC, $|dTEC/dt|$, and rate-of-TEC index (ROTI) over this region at several consecutive epochs are also provided in the supporting information.

The data map shown in Figure 5 captures the spatial distribution of TEC depletions over South America on 10 December 2011 at around 01:03 UTC, with a 3 min integration time. The orientation of these depletions is in general consistent with the expected configuration of equatorial plasma bubbles in the South American sector [*Gentile et al.*, 2006; *Takahashi et al.*, 2014]. Examination of ionogram data taken from around 01:00 UTC on 10 December 2011 reveals that fully developed spread *F* echoes were observed over Fortaleza, Brazil (3.9°S, 38.4°W), which is in agreement with the pattern of TEC depletions shown in Figure 5. Meanwhile, relatively clear ionogram traces and only very light spread echoes were seen over Jicamarca, Peru (12°S, 76.8°W) at that time. A more comprehensive study to compare the spatial distribution of TEC depletions based on this TEC data detrending procedure against ground-based measurements (e.g., ionosondes, incoherent scatter radar, and all-sky imagers) as well as in situ satellite observations (e.g., DMSP, C/NOFS) will be the subject of future investigations.

4. Conclusions

In this paper, we have outlined the concept of a TEC data detrending procedure that could be used effectively to study equatorial plasma bubbles (TEC depletions) as well as AGW/TID. It is based on a mechanical analogy of a large cylindrical barrel rolling on top of a rough terrain to skip over holes/valleys. In theory, the inherent properties drawn from this mechanical analogy would invariably allow this TEC data detrending technique to distinguish between depletions and wavelike features.

In practice, we have also verified that this TEC detrending procedure works quite well and reliably. Through an illustrative example (using a set of real GPS data), we demonstrate how this TEC detrending procedure would function conceptually and realistically under the many imperfections of real experimental data. Furthermore, we extend our discussion to examine a potential implementation of this TEC detrending procedure for geophysical applications. We show that this technique can be utilized to map the detailed geographic profile of TEC depletions associated with equatorial plasma bubbles over a wide and extensive region.

In summary, the capability to distinguish between depletions and wavelike features is crucial in order to accurately infer the overall trend in GPS TEC data. Here we have formulated and demonstrated a reliable way to accomplish this objective via a numerical method. It is hoped that the introduction of this TEC data detrending technique would be able to facilitate significant advancement in space/ionospheric research, and open more doors to new scientific discoveries.

Acknowledgments
This work was supported by FAA grant FAA11-G-006 at Boston College. One of the authors Cesar Valladares was partially supported by Air Force Research Laboratorycontract FA8718-09-C-0041, NSF grants ATM-1135675 and ATM-1242476 and NASA LWS grant NNX11AP02G. The Low Latitude Ionospheric Sensor Network (LISN) is a project led by Boston College in collaboration with the Geophysical Institute of Peru and other institutions that provide information in benefit of the scientific community. We thank all organizations and persons that are supporting and operating receivers in LISN. The TEC values used in this work can be accessed via the LISN web page (http://lisn.igp.gob.pe/). We also thank the University of Massachusetts Lowell Center of Atmospheric Research (UMLCAR) for the ionogram data provided at http://ulcar.uml.edu/DIDBase/.

References

Basu, S., S. Basu, J. Aarons, J. P. McClure, and M. D. Cousins (1978), On the coexistence of kilometer- and meter-scale irregularities in the nighttime equatorial F region, *J. Geophys. Res.*, *83*(A9), 4219–4226, doi:10.1029/JA083iA09p04219.

Borries, C., N. Jakowsky, and V. Wilken (2009), Storm induced large scale TIDs observed in GPS derived TEC, *Ann. Geophys.*, *27*, 1605–1612.

Bromba, M. U. A., and H. Ziegler (1981), Application hints for Savitzky-Golay smoothing filters, *Anal. Chem.*, *53*(11), 1583–1586.

Carter, B. A., A. C. Kellerman, T. A. Kane, P. L. Dyson, R. Norman, and K. Zhang (2013), Ionospheric precursors to large earthquakes: A case study of the 2011 Japanese Tohoku Earthquake, *J. Atmos. Sol. Terr. Phys.*, *102*, 290–297, doi:10.1016/j.jastp.2013.06.006.

Galvan, D. A., A. Komjathy, M. P. Hickey, and A. J. Mannucci (2011), The 2009 Samoa and 2010 Chile tsunamis as observed in the ionosphere using GPS total electron content, *J. Geophys. Res.*, *116*, A06318, doi:10.1029/2010JA016204.

Gentile, L. C., W. J. Burke, and F. J. Rich (2006), A climatology of equatorial plasma bubbles from DMSP 1989-2004, *Radio Sci.*, *41*, RS5S21, doi:10.1029/2005RS003340.

Haase, J. S., T. Dautermann, M. J. Taylor, N. Chapagain, E. Calais, and D. Pautet (2011), Propagation of plasma bubbles observed in Brazil from GPS and airglow data, *Adv. Space Res.*, *47*(10), 1758–1776, doi:10.1016/j.asr.2010.09.025.

Hysell, D. L., M. C. Kelley, W. E. Swartz, R. F. Pfaff, and C. M. Swenson (1994), Steepened structures in equatorial spread F: 1. New observations, *J. Geophys. Res.*, *99*(A5), 8827–8840, doi:10.1029/93JA02961.

Kamogawa, M., and Y. Kakinami (2013), Is an ionospheric electron enhancement preceding the 2011 Tohoku-Oki earthquake a precursor?, *J. Geophys. Res. Space Physics*, *118*, 1751–1754, doi:10.1002/jgra.50118.

Kil, H., and R. A. Heelis (1998), Equatorial density irregularity structures at intermediate scales and their temporal evolution, *J. Geophys. Res.*, *103*(A3), 3969–3981, doi:10.1029/97JA03344.

McClure, J. P., W. B. Hanson, and J. H. Hoffman (1977), Plasma bubbles and irregularities in the equatorial ionosphere, *J. Geophys. Res.*, *82*(19), 2650–2656, doi:10.1029/JA082i019p02650.

Mendillo, M., H. Rishbeth, R. G. Roble, and J. Wroten (2002), Modelling F2-layer seasonal trends and day-to-day variability driven by coupling with the lower atmosphere, *J. Atmos. Sol. Terr. Phys.*, *64*, 1911–1931.

Nicolls, M. J., M. C. Kelley, A. J. Coster, S. A. Gonzalez, and J. J. Makela (2004), Imaging the structure of a large-scale TID using ISR and TEC data, *Geophys. Res. Lett.*, *31*, L09812, doi:10.1029/2004GL019797.

Nishioka, M., T. Tsugawa, M. Kubota, and M. Ishii (2013), Concentric waves and short-period oscillations observed in the ionosphere after the 2013 Moore EF5 tornado, *Geophys. Res. Lett.*, *40*, 5581–5586, doi:10.1002/2013GL057963.

Persson, P.-O., and G. Strang (2003), Smoothing by Savitzky-Golay and legendre filters, in *Mathematical Systems Theory in Biology, Communications, Computation, and Finance*, pp. 301–315, Springer, New York.

Pimenta, A. A., Y. Sahai, J. A. Bittencourt, and F. J. Rich (2007), Ionospheric plasma blobs observed by OI 630 nm all-sky imaging in the Brazilian tropical sector during the major geomagnetic storm of April 6–7, 2000, *Geophys. Res. Lett.*, *34*, L02820, doi:10.1029/2006GL028529.

Pradipta, R., C. E. Valladares, and P. H. Doherty (2014), GPS observation of continent-size traveling TEC pulsations at the start of geomagnetic storms, *J. Geophys. Res. Space Physics*, *119*, 6913–6924, doi:10.1002/2014JA020177.

Rishbeth, H., and M. Mendillo (2001), Patterns of F2-layer variability, *J. Atmos. Sol. Terr. Phys.*, *63*(15), 1661–1680, doi:10.1016/S1364-6826(01)00036-0.

Sambridge, M., J. Braun, and H. McQueen (1995), Geophysical parametrization and interpolation of irregular data using natural neighbours, *Geophys. J. Int.*, *122*, 837–857, doi:10.1111/j.1365-246X.1995.tb06841.x.

Savitzky, A., and M. J. E. Golay (1964), Smoothing and differentiation of data by simplified least squares procedures, *Anal. Chem.*, *36*, 1627–1639.

Seemala, G. K., and C. E. Valladares (2011), Statistics of total electron content depletions observed over the South American continent for the year 2008, *Radio Sci.*, *46*, RS5019, doi:10.1029/2011RS004722.

Sibson, R. (1981), A brief description of natural neighbour interpolation, in *Interpreting Multivariate Data*, edited by V. Barnett, pp. 21–36, Wiley, New York.

Skone, S. (2009), Using GPS TEC measurements to detect geomagnetic Pc 3 pulsations, *Radio Sci.*, *44*, RS0A27, doi:10.1029/2008RS004106.

Takahashi, H., et al. (2014), Diagnostics of equatorial and low latitude ionosphere by TEC mapping over Brazil, *Adv. Space Res.*, *54*(3), 385–394.

Takahashi, H., C. M. Wrasse, Y. Otsuka, A. Ivo, V. Gomes, I. Paulino, A. F. Medeiros, C. M. Denardini, N. Sant'Anna, and K. Shiokawa (2015), Plasma bubble monitoring by TEC map and 630 nm airglow image, *J. Atmos. Sol. Terr. Phys.*, *130-131*, 151–158, doi:10.1016/j.jastp.2015.06.003.

Tsugawa, T., A. Saito, Y. Otsuka, and M. Yamamoto (2003), Damping of large-scale traveling ionospheric disturbances detected with GPS networks during the geomagnetic storm, *J. Geophys. Res.*, *108*(A3), 1127, doi:10.1029/2002JA009433.

Tsugawa, T., Y. Otsuka, A. J. Coster, and A. Saito (2007), Medium-scale traveling ionospheric disturbances detected with dense and wide TEC maps over North America, *Geophys. Res. Lett.*, *34*, L22101, doi:10.1029/2007GL031663.

Tsugawa, T., A. Saito, Y. Otsuka, M. Nishioka, T. Maruyama, H. Kato, T. Nagatsuma, and K. T. Murata (2011), Ionospheric disturbances detected by GPS total electron content observation after the 2011 off the Pacific coast of Tohoku Earthquake, *Earth Planets Space*, *63*, 875–879.